



# Nb<sub>2</sub>O<sub>5</sub>/TiO<sub>2</sub> heterojunctions: Synthesis strategy and photocatalytic activity

Junqing Yan, Guangjun Wu, Naijia Guan, Landong Li\*

Key Laboratory of Advanced Energy Materials Chemistry (Ministry of Education), College of Chemistry, Nankai University, Tianjin 300071, PR China

## ARTICLE INFO

### Article history:

Received 6 November 2013

Received in revised form 22 January 2014

Accepted 26 January 2014

Available online 3 February 2014

### Keywords:

Nb<sub>2</sub>O<sub>5</sub>/TiO<sub>2</sub>

Heterojunction

In situ hydrolysis-loading

Photocatalysis

## ABSTRACT

In the present study, *in situ* hydrolysis-loading of ultra-fine niobium oxide nanoparticles on the surface of rutile TiO<sub>2</sub> is developed as a new strategy to synthesize Nb<sub>2</sub>O<sub>5</sub>/TiO<sub>2</sub> heterojunctions. The physico-chemical properties of Nb<sub>2</sub>O<sub>5</sub>/TiO<sub>2</sub> heterojunctions are fully characterized by X-ray diffraction, Raman, UV-vis, X-ray photoelectron spectroscopy and transmission electron microscopy. The separation efficiency of photo-generated electron-hole pairs on Nb<sub>2</sub>O<sub>5</sub>/TiO<sub>2</sub> heterojunctions under irradiation is investigated by photoluminescence and electron spin resonance spectroscopy. The activity of Nb<sub>2</sub>O<sub>5</sub>/TiO<sub>2</sub> heterojunctions is examined in the selective photocatalytic oxidation of α-phenylethanol and the photocatalytic reforming of methanol. In both reactions, Nb<sub>2</sub>O<sub>5</sub>/TiO<sub>2</sub> heterojunctions exhibit distinct higher photocatalytic activity than pure rutile TiO<sub>2</sub> or Nb<sub>2</sub>O<sub>5</sub>. The photocatalytic activity of Nb<sub>2</sub>O<sub>5</sub>/TiO<sub>2</sub> heterojunctions is relevant with Nb/Ti ratio and the optimal activity is obtained at Nb/Ti = 0.12 with the highest separation efficiency of photo-generated electron-hole pairs. Integrating the physico-chemical and photocatalytic properties, the factors controlling the photocatalytic activity of Nb<sub>2</sub>O<sub>5</sub>/TiO<sub>2</sub> heterojunctions are discussed in detail.

© 2014 Elsevier B.V. All rights reserved.

## 1. Introduction

As a potential process to deal with energy crisis and environmental issues, heterogeneous photocatalysis, known since the 1970s [1], has drawn great attention in the past decades. In heterogeneous photocatalysis, holes in the valence band and electrons in the conducting band are created when the semiconductors are illuminated by photons with energy higher than their band gap. The holes in the valence band are powerful oxidants and the electrons in the conducting band are efficient reductants. Therefore, the photo-generated hole-electron pairs can act as redox centres to initiate photocatalytic reactions [2,3].

TiO<sub>2</sub> is the initial semiconductor photocatalyst investigated, and is still regarded as a benchmark photocatalyst under ultraviolet irradiation. TiO<sub>2</sub> shows several great advantages as photocatalyst, such as good chemical stability, non-toxicity and commercial availability. However, the recombination rate of photo-generated hole-electron pairs on TiO<sub>2</sub> is very high, which greatly reduces the photocatalytic efficiency and limits the industrial application of TiO<sub>2</sub> [4,5]. To address this concern, several strategies have been proposed in the research of TiO<sub>2</sub> photocatalysis, e.g. loading some amounts of metal or metal oxide, known as

co-catalyst, on the surface of TiO<sub>2</sub> [6,7], or combining of TiO<sub>2</sub> with another semiconductor to form heterojunction [8–10]. For these two strategies, the inhibitory effects on recombination of photo-generated hole-electron pairs mainly come from the different Fermi level between TiO<sub>2</sub> and co-catalyst or another semiconductor.

Different types of heterojunctions, e.g. WO<sub>3</sub>/BiVO<sub>4</sub> [11], CdS/TiO<sub>2</sub> [12], Ag<sub>3</sub>PO<sub>4</sub>/BiVO<sub>4</sub> [13] and organic semiconductor heterostructures [14], have been prepared and successfully applied in photocatalysis. In principle, the creation of efficient tight junctions between two semiconductors depends greatly on the synthesis strategy [13]. Delicate design of heterojunctions, e.g. layer-by-layer of WO<sub>3</sub> and BiVO<sub>4</sub> heterojunction electrodes [11] and CaFe<sub>2</sub>O<sub>4</sub> overlayer onto TaON electrode with intimate contact [8], has been proved to be effective to improve the photocatalytic or photoelectrocatalytic activity. Recently, loading ultra-small semiconductor particles on another bulk semiconductor to create heterostructural photocatalysts has been developed to accelerate the charge transfer between the two semiconductor components [15–18]. In this regard, *in situ* creating heterojunction system is reported [13,15,16]. For example, Liu et al. *in situ* loaded ultra-small (*ca.* 2 nm) Cu<sub>2</sub>O particles on TiO<sub>2</sub> nanosheets and the as-prepared Cu<sub>2</sub>O/TiO<sub>2</sub> exhibited photocatalytic activity *ca.* 3 times higher than N-TiO<sub>2</sub> [16]. Yao et al. *in situ* deposited Ag<sub>3</sub>PO<sub>4</sub> nanoparticles onto the TiO<sub>2</sub> surface and Ag<sub>3</sub>PO<sub>4</sub>/TiO<sub>2</sub> exhibited excellent photocatalytic activity [15]. For the *in situ* loading small particles on bulk

\* Corresponding author. Tel.: +86 2223500341.

E-mail address: [lild@nankai.edu.cn](mailto:lild@nankai.edu.cn) (L. Li).

semiconductor, certain conditions are required for the heterogeneous nucleation, e.g. the accurate control of the pH value of the solution [15].

$\text{Nb}_2\text{O}_5$  is n-type transition metal oxide semiconductor with a bad gap of *ca.* 3.2 eV and it has been widely used in photocatalysis [19–22].  $\text{Nb}_2\text{O}_5$ , like  $\text{TiO}_2$ , exhibits good chemical stability, non-toxicity and commercial availability. Therefore,  $\text{Nb}_2\text{O}_5/\text{TiO}_2$  system can be expected as promising composite photocatalyst for application in industrial photocatalysis. To the best of our knowledge, the  $\text{Nb}_2\text{O}_5/\text{TiO}_2$  heterojunction photocatalyst has not been well studied yet. In the present work, we will report the successful synthesis of ultra-fine  $\text{Nb}_2\text{O}_5$  on rutile  $\text{TiO}_2$  via *in situ* hydrolysis-loading under strong acidic conditions and the photocatalytic application of the as-prepared  $\text{Nb}_2\text{O}_5/\text{TiO}_2$  heterojunctions.

## 2. Experimental

### 2.1. Sample preparation

Titanium isopropoxide, isopropanol, niobium(V) chloride (99.9%), benzotrifluoride and  $\alpha$ -phenylethanol were analytical grade and purchased from Alfa Aesar. Nitric acid (26–28 wt%) and hydrochloric acid (36–38%) were provided by Tianjin Guangfu Fine Chemical Research Institute. All the chemical reagents were used as received without further purification. Distilled water was used in the whole experiments.

**Synthesis of rutile  $\text{TiO}_2$  nanoparticles:** Rutile  $\text{TiO}_2$  nanoparticles were synthesized according to previous literature report [23]. Typically, 5 mL of titanium isopropoxide and 5 mL of dry isopropanol were mixed and stirred for 30 min. Then, the solution was added to 40 mL nitric acid solution ( $\text{pH}=0.5$ ). The mixture was heated at 80 °C for 10 h under stirring and the resulting solution was transferred into a 50 mL Teflon-lined autoclave for static crystallization (200 °C for 24 h). The white precipitates were washed thoroughly with distill water and ethanol, and dried at 80 °C overnight. The obtained  $\text{TiO}_2$  powders were annealed at 450 °C for 4 h in air before further use.

**Synthesis of  $\text{Nb}_2\text{O}_5/\text{rutile-TiO}_2$  heterojunctions:** 0.5 g rutile  $\text{TiO}_2$  nanoparticles were dispersed in 30 mL 0.5 M hydrochloric acid solution and the resulting mixture was sonicated for 30 min. Then, a certain amount of  $\text{NbCl}_5$  was added to the mixture under stirring. The homogeneously dispersed solution was heated at 100 °C to obtain the resulting off-white powders. The powders were dried in 80 °C for 24 h and  $\text{Nb}_2\text{O}_5/\text{Rutile-TiO}_2$  heterojunctions were prepared as final products. The products are denoted as  $\text{Nb}/\text{Ti}=n$ , where  $n$  represents the mass ratio of Nb relative to Ti.

Pure  $\text{Nb}_2\text{O}_5$  was also prepared through similar process and used as reference sample.

### 2.2. Sample characterization

The X-ray diffraction (XRD) patterns of samples were recorded on a Bruker D8 ADVANCE powder diffractometer using  $\text{Cu-K}\alpha$  radiation ( $\lambda=0.1542 \text{ nm}$ ) at a scanning rate of  $4 \text{ min}^{-1}$  in the region of  $2\theta=10\text{--}80^\circ$ .

The specific surface areas of samples were determined through low temperature  $\text{N}_2$  adsorption/desorption isotherms collected on a Quantachrome iQ-MP gas adsorption analyzer.

Transmission electron microscopy (TEM) images were taken on a Philips Tecnai G<sup>2</sup> 20 S-TWIN electron microscope at an acceleration voltage of 200 kV. A few drops of alcohol suspension containing the sample were placed on a carbon-coated copper grid, followed by evaporation at ambient temperature.

Raman analysis was carried out on a Renishaw InVia Raman spectrometer and spectra were obtained with the green line of an Ar-ion laser (514.53 nm) in micro-Raman configuration.

Diffuse reflectance ultraviolet-visible (UV-Vis) spectra of diluted samples (diluted in  $\text{BaSO}_4$  at a ratio of 1:9) were recorded in the air against  $\text{BaSO}_4$  in the region of 200–700 nm on a Varian Cary 300 UV-vis spectrophotometer.

X-ray photoelectron spectra (XPS) were recorded on a Kratos Axis Ultra DLD spectrometer with a monochromated Al-K $\alpha$  X-ray source ( $h\nu=1486.6 \text{ eV}$ ), hybrid (magnetic/electrostatic) optics and a multi-channel plate and delay line detector (DLD). All spectra were recorded by using an aperture slot of  $300\times 700$  microns, survey spectra were recorded with a pass energy of 160 eV and high-resolution spectra with a pass energy of 40 eV. Accurate binding energies ( $\pm 0.1 \text{ eV}$ ) were determined with respect to the position of the adventitious C 1s peak at 284.8 eV.

Photoluminescence (PL) spectra were recorded on a Spex FL201 fluorescence spectrophotometer. The samples were dry-pressed into self-supporting wafers and then illuminated by 325 nm He-Cd laser as excitation source at ambient temperature.

Electron spin resonance (ESR) was carried out on a Bruker A300 instrument with a microwave power of 5.0 mW and a modulation frequency of 100 kHz. 2,2-Diphenyl-1-picrylhydrazyl hydrate (DPPH) was used as an internal standard for the measurement of the magnetic field. In a typical experiment, sample of 0.15 g was placed in a quartz ESR tube and evacuated at 473 K for 2 h. After cooled down to 298 K, 50 Torr  $\text{O}_2$  was introduced to the cube and kept for 15 min. The excess amount of  $\text{O}_2$  was removed from the tube by evacuation for 10 min and then the tube was analyzed at 100 K in dark or under UV-vis light irradiation.

Mott-Schottky plots were measured using a three-electrode cell electrochemical workstation (VIUUM CompactStat). The saturated Ag/AgCl and platinum foil ( $2\times 2 \text{ cm}^2$ ) were used as the reference electrode and the counter electrode. The sample (1 mg) was dispersed in 1 mL anhydrous ethanol and then evenly grinded to slurry. The slurry was spread onto ITO glass and the exposed area was kept at  $0.25 \text{ cm}^2$ . The prepared ITO/samples was dried overnight under ambient conditions and then used as the working electrode. The measurements were obtained at a fixed frequency of 1 kHz in 0.5 M  $\text{Na}_2\text{SO}_4$  solution in the dark.

### 2.3. Photocatalytic evaluation

The photocatalytic oxidation of  $\alpha$ -phenylethanol was performed in a top-irradiation-type double-walled quartz cell cooled by water with a Xe lamp (200 W, wavelength: 320–780 nm) as a light source. In each experiment, the catalyst of *ca.* 0.3 g was dispersed in the mixture of benzotrifluoride (solvent) and 25 mmol  $\alpha$ -phenylethanol (or other alcohol) in the quartz cell under stirring. The suspension was then irradiated with air bubbled in at *ca.* 20 mL/min. The organic products were analyzed by GC (Shimadzu GC-2010 Plus) and GC-MS (Shimadzu GCMS-QP2010 SE). Meanwhile, an absorption apparatus containing saturated  $\text{Ba}(\text{OH})_2$  solution was equipped at down-stream of quartz cell to determine the quantity of  $\text{CO}_2$  that might form during reaction.

Photocatalytic reforming of methanol (also-known as photocatalytic water splitting with methanol as sacrificial agent) was performed in a top-irradiation-type Pyrex reaction cell connected to a closed gas circulation and evacuation system under the irradiation of Xe lamp (wavelength: 320–780 nm). In a typical experiment, catalyst sample of 100 mg was suspended in 100 mL 10% methanol aqueous solution in the reaction cell. After evacuated for 30 min, the reactor cell was irradiated by the Xe lamp at 200 W under stirring. The gaseous products were analyzed by an on-line gas chromatograph (Varian CP-3800) with thermal conductivity

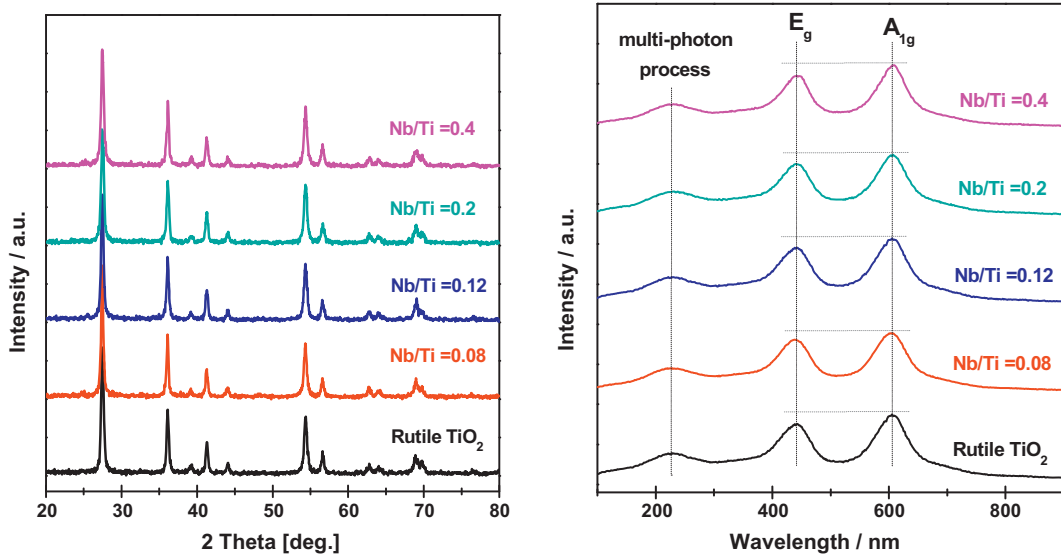


Fig. 1. XRD (left) and Raman (right) patterns of rutile  $\text{TiO}_2$  and Nb<sub>2</sub>O<sub>5</sub>/TiO<sub>2</sub> heterojunctions.

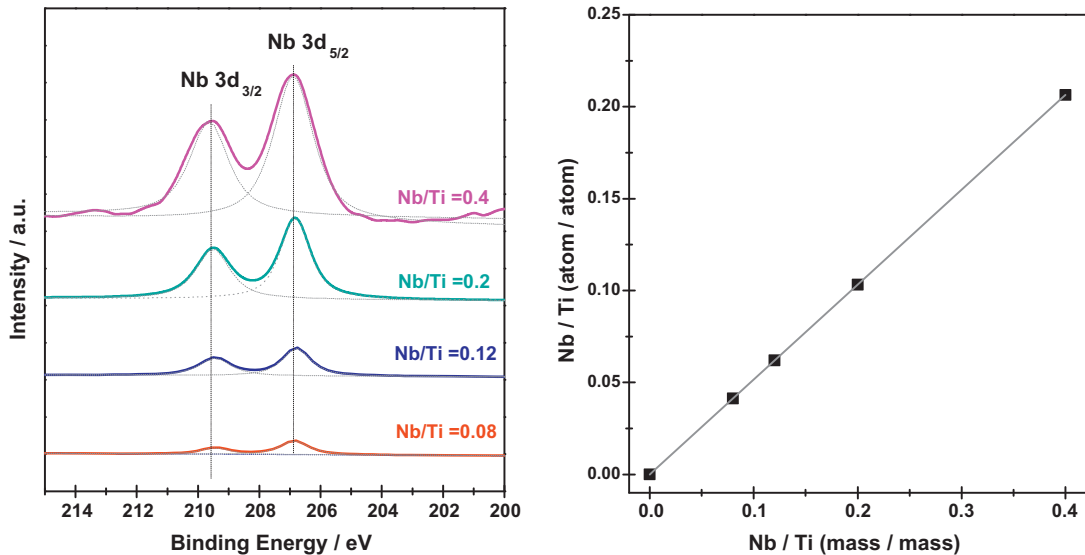


Fig. 2. XPS (left) and surface niobium loadings (right) of Nb<sub>2</sub>O<sub>5</sub>/TiO<sub>2</sub> heterojunctions.

detector. For all photocatalyst samples, 1% Pt was *in situ* photo-deposited from H<sub>2</sub>PtCl<sub>6</sub> solution.

### 3. Results and discussion

#### 3.1. Formation and characterization of Nb<sub>2</sub>O<sub>5</sub>/TiO<sub>2</sub> heterojunctions

The phase structure of rutile  $\text{TiO}_2$  and Nb<sub>2</sub>O<sub>5</sub>/TiO<sub>2</sub> heterojunctions are characterized by XRD and Raman spectroscopy. As shown in Fig. 1 (left), the typical diffraction patterns of rutile  $\text{TiO}_2$  (JCPDF# 21-1276) are observed for  $\text{TiO}_2$  and Nb<sub>2</sub>O<sub>5</sub>/TiO<sub>2</sub> heterojunctions. Besides, no diffraction peaks corresponding to niobium species could be observed, which should be due to the high dispersion of niobium species and their amorphous state (Fig. S1) [20,22]. On the other hand, the intensities and shapes of diffraction peaks are quite similar, and the average particle sizes are calculated to *ca.* 30 nm for all samples according to the Scherer equation from the broadening of rutile (110) reflection ( $2\theta = 27.5$ ). Raman spectra

are further employed to identify the surface geometric structure of the samples. As shown in Fig. 1 (right), three Raman-active modes corresponding to the typical vibrational bands of rutile  $\text{TiO}_2$  [24] are clearly observed for  $\text{TiO}_2$  and Nb<sub>2</sub>O<sub>5</sub>/TiO<sub>2</sub> heterojunctions. The absence of Raman-active modes corresponding to niobium oxides in Nb<sub>2</sub>O<sub>5</sub>/TiO<sub>2</sub> heterojunctions indicates that Nb<sub>2</sub>O<sub>5</sub> is amorphous. Moreover, the unchanged Raman-active modes before and after Nb<sub>2</sub>O<sub>5</sub> loading suggest that loading of Nb<sub>2</sub>O<sub>5</sub> on  $\text{TiO}_2$  do not influence the surface structure of rutile  $\text{TiO}_2$ .

The existence states of niobium species and surface elemental composition in Nb<sub>2</sub>O<sub>5</sub>/TiO<sub>2</sub> heterojunctions are investigated by means of XPS and the results are shown in Fig. 2. Ti, O and Nb are detected as exclusive elements in Nb<sub>2</sub>O<sub>5</sub>/TiO<sub>2</sub> heterojunctions (Fig. S2), ruling out the possible influences from impurities. In Nb 3d region, the binding energy values at 207.1 and 209.9 eV are observed for pure Nb<sub>2</sub>O<sub>5</sub> sample (Fig. S3), confirming that amorphous Nb<sub>2</sub>O<sub>5</sub> is obtained as reference sample. While for Nb<sub>2</sub>O<sub>5</sub>/TiO<sub>2</sub> heterojunctions, the binding energy values at 206.9 and 209.7 eV are observed, which are *ca.* 0.2 eV lower than reference Nb<sub>2</sub>O<sub>5</sub>

**Table 1**

Physicochemical properties of rutile TiO<sub>2</sub> and Nb<sub>2</sub>O<sub>5</sub>/TiO<sub>2</sub> heterojunctions.

Samples	Niobium loading <sup>a</sup>	TiO <sub>2</sub> size <sup>b</sup>	Nb <sub>2</sub> O <sub>5</sub> size <sup>c</sup>	BET surface area
Rutile TiO <sub>2</sub>	0%	32.1 nm	—	58.2 m <sup>2</sup> g <sup>-1</sup>
Nb/Ti = 0.08	4.8%	33.2 nm	2.1 nm	56.7 m <sup>2</sup> g <sup>-1</sup>
Nb/Ti = 0.12	7.2%	32.3 nm	2.2 nm	57.3 m <sup>2</sup> g <sup>-1</sup>
Nb/Ti = 0.2	12.1%	30.5 nm	2.4 nm	56.8 m <sup>2</sup> g <sup>-1</sup>
Nb/Ti = 0.4	23.9%	31.3 nm	2.5 nm	54.9 m <sup>2</sup> g <sup>-1</sup>

<sup>a</sup> Determined by ICP.

<sup>b</sup> Estimated by Scherer equation from the broadening of rutile (110) reflection in XRD.

<sup>c</sup> Estimated by TEM observations.

ca. 0.9 eV higher than NbO<sub>2</sub> [25,26]. Based on the Nb 3d XPS results, we propose that niobium species exist in the form of electron-rich Nb<sub>2</sub>O<sub>5</sub> in Nb<sub>2</sub>O<sub>5</sub>/TiO<sub>2</sub> heterojunctions. The excess electrons should come from the defect sites in TiO<sub>2</sub> support and Nb<sub>2</sub>O<sub>5</sub>-TiO<sub>2</sub> interaction (vide infra). Other important information we can obtain from XPS analysis is the surface composition of Nb<sub>2</sub>O<sub>5</sub>/TiO<sub>2</sub> heterojunctions in the depth up to several nanometers and surface niobium loadings are displayed in Fig. 2 (right). It is seen that surface niobium loading is obvious higher than bulk niobium loading determined by ICP (Table 1) and the surface niobium loading increases distinctly with increasing bulk Nb/Ti ratio, indicating the surface enrichment of homogeneously dispersed niobium species in Nb<sub>2</sub>O<sub>5</sub>/TiO<sub>2</sub> heterojunctions. Integrating the characterization results from XRD, Raman and TEM (vide infra), we can conclude that the in situ loaded niobium species on the surface rutile TiO<sub>2</sub> are well-dispersed amorphous Nb<sub>2</sub>O<sub>5</sub> nanoparticles.

Diffuse reflectance UV-vis spectroscopy was performed to study the optical properties of rutile TiO<sub>2</sub>, amorphous Nb<sub>2</sub>O<sub>5</sub> and Nb<sub>2</sub>O<sub>5</sub>/TiO<sub>2</sub> heterojunctions. For rutile TiO<sub>2</sub>, intrinsic absorption in the ultraviolet region attributed to the band-band transition is observed (Fig. 3) and the band gap energy is estimated to be 3.05 eV [10]. For amorphous Nb<sub>2</sub>O<sub>5</sub>, intrinsic absorption in the ultraviolet region attributed to the band-band transition is observed and gap energy is estimated to be 3.35 eV. While for Nb<sub>2</sub>O<sub>5</sub>/TiO<sub>2</sub> heterojunctions, intrinsic absorption in the ultraviolet region are also observed and the absorption edges appear in the region of 410–415 nm. That is to say, loading of Nb<sub>2</sub>O<sub>5</sub> on the surface of TiO<sub>2</sub> does not significantly change the intrinsic absorption of rutile TiO<sub>2</sub> (the small red shift could be neglected). Besides, noticeable decreases in the light

absorption in ultraviolet region can be observed, which might be associated with interface charge transfer between TiO<sub>2</sub> and Nb<sub>2</sub>O<sub>5</sub>. In the Marcus theory, when the particle size of the semiconductor is very small (e.g. 3 nm), the electrons transfer across the semiconductor interface will be greatly accelerated and the apparent light absorption decreases [27].

Transmission electron microscopy (TEM) was employed to study the morphology of rutile TiO<sub>2</sub> and Nb<sub>2</sub>O<sub>5</sub>/TiO<sub>2</sub> heterojunctions, and the results are showed in Fig. 4. The average particle size of rutile TiO<sub>2</sub> particles is observed to be ca. 30 nm, in great consistence with XRD analysis results. For Nb<sub>2</sub>O<sub>5</sub>/TiO<sub>2</sub> heterojunctions, dark dots of 2–3 nm are clearly observed on the surface of rutile TiO<sub>2</sub> particles. Energy dispersive spectroscopy (EDS) analysis results confirm that the dark dots are niobium-containing species, i.e. Nb<sub>2</sub>O<sub>5</sub> nanoparticles (Fig. 4f, Fig. S4). The Nb<sub>2</sub>O<sub>5</sub> nanoparticles are uniform with very narrow size distributions, not so relevant with the niobium loading. Obviously, no core-shell structure can be detected even at high niobium loadings, in great contrast to literature reports [28].

For a direct view, some relevant physicochemical properties of rutile TiO<sub>2</sub> and Nb<sub>2</sub>O<sub>5</sub>/TiO<sub>2</sub> heterojunctions are summarized in Table 1.

Based on above-mentioned experimental results, the formation mechanism of Nb<sub>2</sub>O<sub>5</sub>/TiO<sub>2</sub> heterojunctions can be described as follows. In the first step, rutile TiO<sub>2</sub> nanoparticles are well dispersed in the strong acid solution (0.5 M HCl) with pH value of ca. 0.4, far away from the isoelectric point (IEP) of rutile TiO<sub>2</sub> particles (6–7) [29], which can provide a pledge for the homogeneous dispersion of Nb<sub>2</sub>O<sub>5</sub> particles. Moreover, the surface of TiO<sub>2</sub> could be positively charged due to surface adsorption of proton [30], which can promote the absorptivity of anions on the surface of TiO<sub>2</sub>. In the second step, when NbCl<sub>5</sub> is added into 30 mL 0.5 M hydrochloric acid solution, a series of negatively charged hydrolyzed products, such as Nb(OH)<sub>2</sub>Cl<sub>4</sub><sup>−</sup> anions, come into being and clear solution is formed (Fig. 4h). In control experiments, NbCl<sub>5</sub> is added into 30 mL aqueous solution and a cloudy solution is obtained (Fig. 4g), indicating that water-insoluble niobium hydroxide is formed. Here the use of strong acidic mediate is a must to obtain clear solution containing niobium anions. In the mixed strong acidic solution containing both rutile TiO<sub>2</sub> and hydrolyzed niobium ions, negatively charged hydrolyzed niobium anions will absorb on the surface of TiO<sub>2</sub>. In the last step, the mixture was heated to 100 °C to remove water

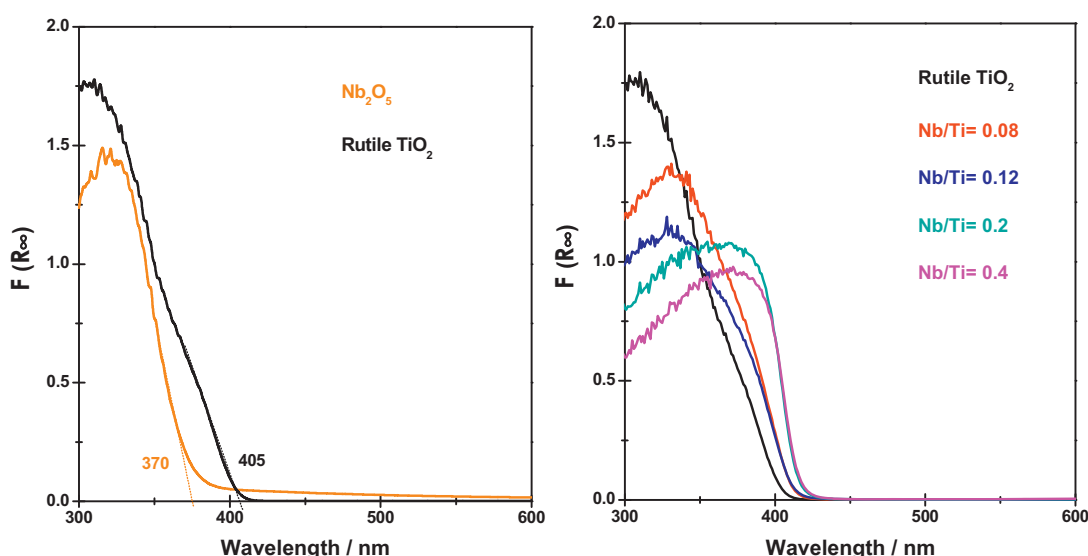
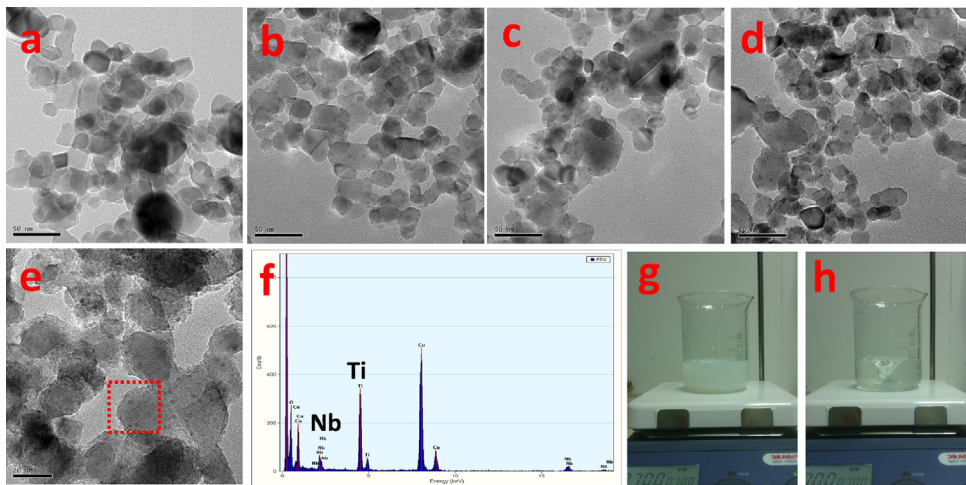
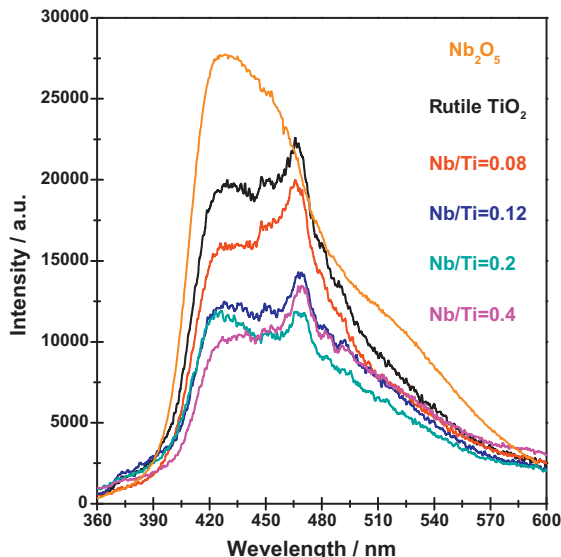


Fig. 3. UV-vis spectra of TiO<sub>2</sub>, Nb<sub>2</sub>O<sub>5</sub> and as-synthesized Nb<sub>2</sub>O<sub>5</sub>/TiO<sub>2</sub> heterojunctions.



**Fig. 4.** TEM images of rutile TiO<sub>2</sub> (a) and Nb<sub>2</sub>O<sub>5</sub>/TiO<sub>2</sub> heterojunctions: Nb/Ti = 0.08 (b), Nb/Ti = 0.12 (c), Nb/Ti = 0.2 (d), Nb/Ti = 0.4 (e); EDS analysis on the red zone in e (f); Photographs of 0.5 g NbCl<sub>5</sub> in 30 mL distill water (g) and 0.5 M HCl aqueous solution (h).



**Fig. 5.** PL spectra of rutile TiO<sub>2</sub> and Nb<sub>2</sub>O<sub>5</sub>/TiO<sub>2</sub> heterojunctions recorded at room temperature.

and hydrochloric acid, and Nb<sub>2</sub>O<sub>5</sub> nanoparticles are *in situ* loaded on the surface of rutile TiO<sub>2</sub>.

PL spectroscopy is very useful to disclose the efficiency of charge carrier trapping, immigration and transfer in semiconductor. Generally, the PL emissions are originated from the radiative recombination of photo-generated electrons–holes [31–33]. Room temperature emission PL spectra of rutile TiO<sub>2</sub> and Nb<sub>2</sub>O<sub>5</sub>/TiO<sub>2</sub> heterojunctions are shown in Fig. 5. Two obvious signals at *ca.* 430 and 465 nm are observed for TiO<sub>2</sub> and all Nb<sub>2</sub>O<sub>5</sub>/TiO<sub>2</sub> heterojunctions, originated from the irradiative recombination of free electrons in shallow traps and sub-bands below conductive band and free holes at the valance band edge [32–34]. The intensities of the two PL signals are greatly reduced with the *in situ* loading of Nb<sub>2</sub>O<sub>5</sub> on TiO<sub>2</sub> surface, indicating that heterojunctions formation can effectively suppress the irradiative recombination. Therefore, the Nb<sub>2</sub>O<sub>5</sub>/TiO<sub>2</sub> heterojunctions are expected to exhibit promoted activity in photocatalytic reactions.

Electron spin resonance (ESR) spectroscopy is employed to obtain more information about our Nb<sub>2</sub>O<sub>5</sub>/TiO<sub>2</sub> heterojunctions and the results are showed in Fig. 6. From the ESR results in the dark, only one weak peak ( $g=2.001$ ) is detected for pure rutile

TiO<sub>2</sub> and Nb<sub>2</sub>O<sub>5</sub>/TiO<sub>2</sub> (no signal can be detected for reference Nb<sub>2</sub>O<sub>5</sub> sample), which should be attributed to O<sup>−</sup> from O<sub>2</sub> dissociative adsorption onto the surface oxygen vacancy sites of TiO<sub>2</sub> [35,36]. After normalization, the intensity of the O<sup>−</sup> signal decreases with increasing niobium loading on the surface of TiO<sub>2</sub>, indicating the mask of the surface defect sites of TiO<sub>2</sub> by niobium loading [36]. That is, the surface defect sites of rutile TiO<sub>2</sub> are the nucleation centers for niobium precursor and the heterogeneous distribution of Nb<sub>2</sub>O<sub>5</sub> are therefore ensured. This is the reason for the formation of electron-rich Nb<sub>2</sub>O<sub>5</sub> as revealed by XPS analysis (Fig. 2).

On the other hand, more ESR signals appear for all samples under UV-Vis irradiation. The intense signals consisting of three sets of rhombic *g* values could be assigned to superoxide species (O<sub>2</sub><sup>−</sup>:  $g_1 = 2.002$ ,  $g_2 = 2.009$ ,  $g_3 = 2.028$ ), which are formed via the reduction of adsorbed O<sub>2</sub> by excited electrons [28]. After normalization, the intensities of the superoxide species on Nb<sub>2</sub>O<sub>5</sub>/TiO<sub>2</sub> heterojunctions are much higher than those on rutile TiO<sub>2</sub> and Nb<sub>2</sub>O<sub>5</sub>. For Nb<sub>2</sub>O<sub>5</sub>/TiO<sub>2</sub> heterojunctions, the intensities of superoxide species increase with increasing niobium loading, reach a maximum at Nb/Ti = 0.2, and then begin to decrease. The higher intensity of superoxide species corresponds to higher separation efficiency of photo-generated electron-hole pairs, in consistence with PL results in Fig. 5. Besides the superoxide species, two signals can be observed at  $g = 1.982$  and 1.978 under irradiation, corresponding to the bulk Ti<sup>3+</sup> species [28]. The higher intensities of bulk Ti<sup>3+</sup> species may also indicate the higher separation efficiency of photo-generated electron-hole pairs on Nb<sub>2</sub>O<sub>5</sub>/TiO<sub>2</sub> heterojunctions than that on rutile TiO<sub>2</sub>.

### 3.2. Photocatalytic activity of Nb<sub>2</sub>O<sub>5</sub>/TiO<sub>2</sub> heterojunctions

The photocatalytic activities of the as-prepared pure rutile TiO<sub>2</sub> and Nb<sub>2</sub>O<sub>5</sub>/TiO<sub>2</sub> heterojunctions are evaluated in the photocatalytic oxidation  $\alpha$ -phenethyl alcohol, and the results are showed in Fig. 7. The selective photocatalytic oxidation of  $\alpha$ -phenethyl alcohol can be achieved on all catalysts with selectivity of >95% to acetophenone (dehydroxylated toluene as detectable by-product), in accordance with our previous results over anatase and rutile TiO<sub>2</sub> [5]. The photocatalytic activities in Fig. 7 clearly indicate that Nb<sub>2</sub>O<sub>5</sub>/TiO<sub>2</sub> heterojunctions exhibit higher activity than pure rutile TiO<sub>2</sub> and Nb<sub>2</sub>O<sub>5</sub>. For Nb<sub>2</sub>O<sub>5</sub>/TiO<sub>2</sub> heterojunctions, the photocatalytic activity first increases with increasing niobium loading, reaches a maximal at Nb/Ti = 0.12 and then begins to decrease.

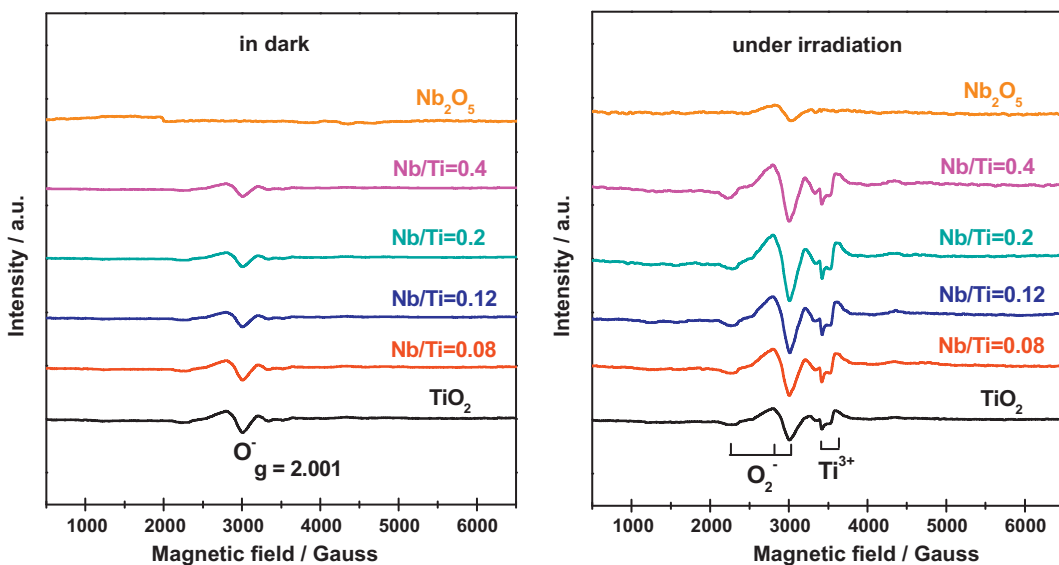


**Fig. 6.** ESR spectra of  $\text{TiO}_2$  and  $\text{Nb}_2\text{O}_5/\text{TiO}_2$  heterojunctions in the dark and under irradiation.

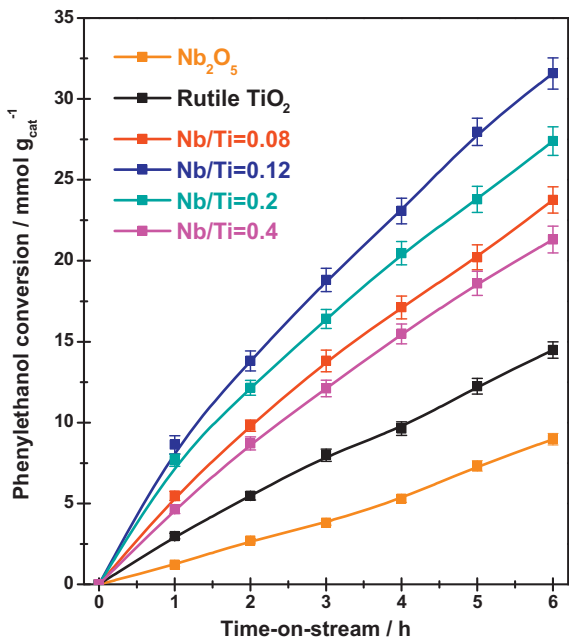


**Fig. 7.** The photocatalytic oxidation  $\alpha$ -phenylethanol over rutile  $\text{TiO}_2$  and  $\text{Nb}_2\text{O}_5/\text{TiO}_2$  heterojunctions under UV-Vis light irradiation; Reaction conditions: catalyst 0.3 g;  $\alpha$ -phenethyl alcohol 25 mmol, benzotrifluoride 27 mL.

The highest  $\alpha$ -phenethyl alcohol photocatalytic oxidation rate of *ca.* 8  $\text{mmol g}_{\text{cat}}^{-1} \text{h}^{-1}$ , three times higher than rutile  $\text{TiO}_2$  or eight times higher than  $\text{Nb}_2\text{O}_5$ , is obtained on  $\text{Nb}_2\text{O}_5/\text{TiO}_2$  heterojunction at  $\text{Nb}/\text{Ti} = 0.12$ . Since the specific surface areas of all the samples are quite similar (Table 1), the mass specific activity can reflect the intrinsic activity, *i.e.* the surface specific activity [37], quite well.

Our  $\text{Nb}_2\text{O}_5/\text{TiO}_2$  heterojunctions also exhibit good recycling ability in the photocatalytic oxidation  $\alpha$ -phenylethanol (results not shown here). XPS analysis results reveal that the existence states of niobium and titanium are kept unchanged after reaction (Fig. S5), confirming that  $\text{Nb}_2\text{O}_5/\text{TiO}_2$  heterojunctions act as photocatalyst during reaction.

Initiated by the superior activity of  $\text{Nb}_2\text{O}_5/\text{TiO}_2$  heterojunctions for the photocatalytic oxidation of  $\alpha$ -phenethyl alcohol, we further investigated the photocatalytic oxidation of

various aromatic alcohols over  $\text{Nb}_2\text{O}_5/\text{TiO}_2$ . As shown in Table 2,  $\text{Nb}_2\text{O}_5/\text{TiO}_2$  ( $\text{Nb}/\text{Ti} = 0.12$ ) exhibits high activity for the photocatalytic oxidation of aromatic alcohols as well as good selectivity to carbonyl compounds in most cases. Exceptionally, the photocatalytic oxidation of diphenylmethanol over  $\text{Nb}_2\text{O}_5/\text{TiO}_2$  is very slow because the adsorption of diphenylmethanol onto catalyst is difficult due to steric hindrance. For the photocatalytic oxidation of para-substituted benzyl alcohols, the activity is governed by the Hammett rule, *i.e.* substitution with electron-releasing groups  $-\text{OCH}_3$  and  $-\text{CH}_3$  increases the activity while substitution with electron-releasing groups  $-\text{Cl}$  and  $-\text{NO}_2$  decreases the activity. In all cases, the photocatalytic activity of  $\text{Nb}_2\text{O}_5/\text{TiO}_2$  is several times higher than reference rutile  $\text{TiO}_2$ , demonstrating the advantage of heterojunctions formation. It should be mentioned that aldehyde selectivity in the photocatalytic oxidation of primary aromatic alcohols is relatively low because the successive photocatalytic oxidation of product aldehydes to carboxylic acids and subsequent esterification between alcohols and carboxylic acids cannot be avoided under our reaction conditions.

The photocatalytic activities of the as-prepared pure rutile  $\text{TiO}_2$  and  $\text{Nb}_2\text{O}_5/\text{TiO}_2$  heterojunctions are also evaluated in the photocatalytic methanol reforming, and the results are shown in Fig. 8. Rutile  $\text{TiO}_2$  (with 1 wt% Pt as co-catalyst) exhibits considerable photocatalytic activity in the methanol reforming, while amorphous  $\text{Nb}_2\text{O}_5$  exhibits relatively lower photocatalytic activity, in consistence with literature reports [20,22,38,39]. For  $\text{Nb}_2\text{O}_5/\text{TiO}_2$  heterojunctions, considerable hydrogen evolution rates from methanol reforming are observed and  $\text{Nb}/\text{Ti}$  ratios can influence the photocatalytic activity to some extent. Typically, the photocatalytic activity in methanol reforming first increases with increasing niobium loading, reaches a maximal at  $\text{Nb}/\text{Ti}$  ratio of 0.12 and then begins to decrease, similar to that in the photocatalytic oxidation  $\alpha$ -phenylethanol. The highest hydrogen evolution rate of *ca.* 1.8  $\text{mmol g}_{\text{cat}}^{-1} \text{h}^{-1}$  is obtained on  $\text{Nb}_2\text{O}_5/\text{TiO}_2$  ( $\text{Nb}/\text{Ti} = 0.12$ ), which is less than two times higher as rutile  $\text{TiO}_2$  (1.0  $\text{mmol g}_{\text{cat}}^{-1} \text{h}^{-1}$ ). Comparing the activities of  $\text{Nb}_2\text{O}_5/\text{TiO}_2$  heterojunctions in the photocatalytic oxidation  $\alpha$ -phenylethanol and photocatalytic methanol reforming, we can conclude that heterojunctions can promote the photocatalytic activity in both reactions while the promotion effects are somewhat different, which will be discussed in the following section.

**Table 2**Aerobic oxidation of aromatic alcohols over  $\text{Nb}_2\text{O}_5/\text{TiO}_2$  and bare  $\text{TiO}_2$ <sup>a</sup>.

Entry	Substrate	Product	Catalyst	Conversion (%) <sup>b</sup>	Selectivity (%) <sup>c</sup>	Reaction rate ( $\text{mmol g}_{\text{cat}}^{-1} \text{h}^{-1}$ )
1			$\text{Nb}_2\text{O}_5/\text{TiO}_2$ $\text{TiO}_2$	64.3 21.6	85.1 91.4	16.4 5.4
2			$\text{Nb}_2\text{O}_5/\text{TiO}_2$ $\text{TiO}_2$	66.2 23.1	84.9 90.3	17.1 5.9
3			$\text{Nb}_2\text{O}_5/\text{TiO}_2$ $\text{TiO}_2$	67.8 24.9	74.3 93.1	17.6 6.2
4			$\text{Nb}_2\text{O}_5/\text{TiO}_2$ $\text{TiO}_2$	29.3 10.2	85.6 91.5	7.6 2.7
5			$\text{Nb}_2\text{O}_5/\text{TiO}_2$ $\text{TiO}_2$	12.3 5.8	83.9 94.3	3.6 1.5
6			$\text{Nb}_2\text{O}_5/\text{TiO}_2$ $\text{TiO}_2$	60.5 24.2	94.8 96.7	15.7 7.2
7			$\text{Nb}_2\text{O}_5/\text{TiO}_2$ $\text{TiO}_2$	31.2 13.1	96.3 97.2	8.0 2.6
8			$\text{Nb}_2\text{O}_5/\text{TiO}_2$ $\text{TiO}_2$	3.2 0.9	97.4 98.1	0.9 0.3

<sup>d</sup>Calculated at aromatic alcohol conversion of 10–15%.<sup>a</sup> Reaction conditions: 0.3 g catalyst, 25 mmol aromatic alcohol, 27 mL benzotrifluoride.<sup>b</sup> Aromatic alcohol conversion at time-on-stream of 5 h.<sup>c</sup> Aldehyde or ketone selectivity at time-on-stream of 5 h.

### 3.3. Factors controlling the photocatalytic activity of $\text{Nb}_2\text{O}_5/\text{TiO}_2$ heterojunctions

The UV–Vis spectra indicate the acceleration of electrons transfer across the semiconductor interface originated from the heterojunctions, which should be responsible for the promotion of photocatalytic activity of  $\text{Nb}_2\text{O}_5/\text{TiO}_2$  heterojunctions compared with rutile  $\text{TiO}_2$  or  $\text{Nb}_2\text{O}_5$ . However, over-high Nb/Ti ratio will lead to the decrease in the photocatalytic activity because too many heterojunctions can also act as the recombination sites for photo-generated electron–hole pairs [40]. As a balance of these two factors, a proper amount of heterojunctions should correspond to the best photocatalytic activity. In the present study, the Nb/Ti ratio of 0.12 could be optimized for  $\text{Nb}_2\text{O}_5/\text{TiO}_2$  heterojunctions in both photocatalytic oxidation of  $\alpha$ -phenylethanol (Fig. 7) and photocatalytic reforming of methanol (Fig. 8).

For amorphous  $\text{Nb}_2\text{O}_5$  semiconductor, the conduction band potential is reported to be at least 0.2 eV positive, relative to anatase

$\text{TiO}_2$  [21,41]. However, the relative band edge positions between amorphous  $\text{Nb}_2\text{O}_5$  and rutile  $\text{TiO}_2$  have not been reported. So, we predict theoretically the band edge positions of the conduction band ( $E_{\text{CB}}$ ) and valence band ( $E_{\text{VB}}$ ) of the two semiconductors at the point of zero charge using the following empirical equation [42,43]:

$$E_{\text{CB}} = X - E^e - 0.5E_g$$

$$E_{\text{VB}} = E_g - E_{\text{CB}}$$

Here,  $X$  is the absolute electronegativity of the semiconductor, obtained from the geometric mean of the electronegativity of its constituent atoms ( $X$  values for  $\text{Nb}_2\text{O}_5$  and  $\text{TiO}_2$  are 5.55 and 5.81, respectively [43]);  $E_g$  is the band gap of the semiconductor;  $E^e$  is the energy of free electrons on the hydrogen scale (4.5 eV). The calculated conduction band edge potential of amorphous  $\text{Nb}_2\text{O}_5$  ( $-0.45$  eV) is more negative than that of rutile  $\text{TiO}_2$  ( $-0.19$  eV) and

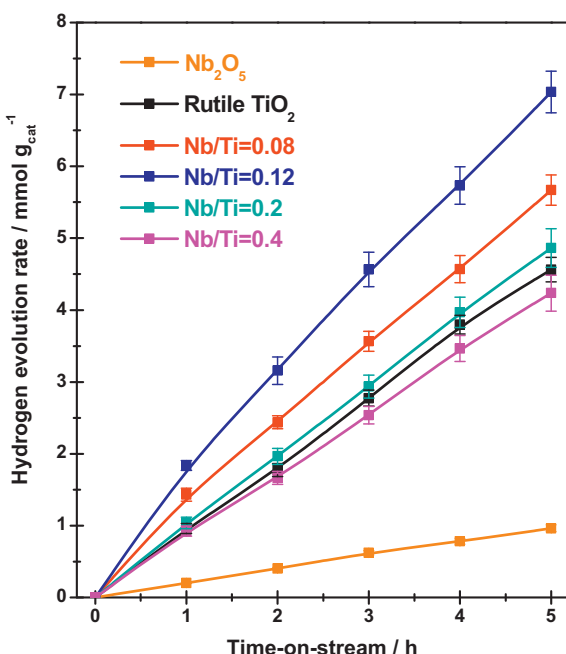


**Fig. 8.** Photocatalytic hydrogen evolution from methanol reforming over rutile  $\text{TiO}_2$  and  $\text{Nb}_2\text{O}_5/\text{TiO}_2$  heterojunctions under UV-vis light irradiation; 1 wt% Pt is *in situ* photo-deposited on the surface of samples.

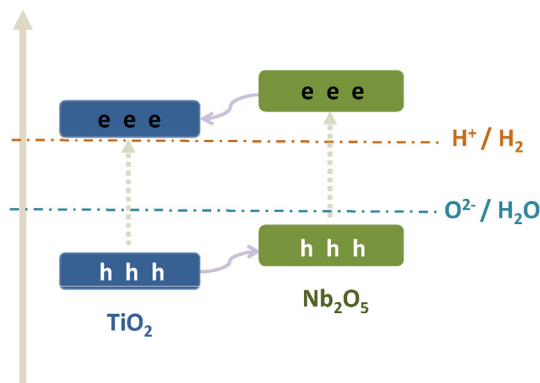


**Fig. 9.** Schematic diagram of  $\text{Nb}_2\text{O}_5/\text{TiO}_2$  heterojunction and the relative conduction and valence band structure; Transfer directions of the photo-generated electrons and holes are also given.

the corresponding valence band edge potential of  $\text{TiO}_2$  (2.81 eV) is more than that of  $\text{Nb}_2\text{O}_5$  (2.75 eV). Therefore, when electron–hole pairs are created on semiconductor heterojunction upon ultraviolet light irradiation, the photo-generated electrons in the conduction band of  $\text{Nb}_2\text{O}_5$  can transfer to rutile  $\text{TiO}_2$ , and the photo-generated holes are reversely transferred under the driving force of Fermi energy difference between the two semiconductors [14,44]. The schematic diagram of  $\text{Nb}_2\text{O}_5/\text{TiO}_2$  heterojunction system and the transfer direction of the photo-generated electrons and holes are described in Fig. 9.

To further address the relative band structure of  $\text{TiO}_2$  and  $\text{Nb}_2\text{O}_5$  in this study, we measured the flat-band potentials using the electrochemical method [45,46] and the Mott–Schottky plots are shown in Fig. 10. It can be seen that both  $\text{TiO}_2$  and  $\text{Nb}_2\text{O}_5$  show positive slopes, confirming the fact that they are n-type semiconductors. Obviously, the  $E_{\text{cb}}$  of  $\text{Nb}_2\text{O}_5$  is more negative than that of  $\text{TiO}_2$ , which is in good agreement with the data of the above-mentioned calculation results [47]. The Mott–Schottky plots of  $\text{Nb}_2\text{O}_5/\text{TiO}_2$  heterojunctions are quite similar and the slope

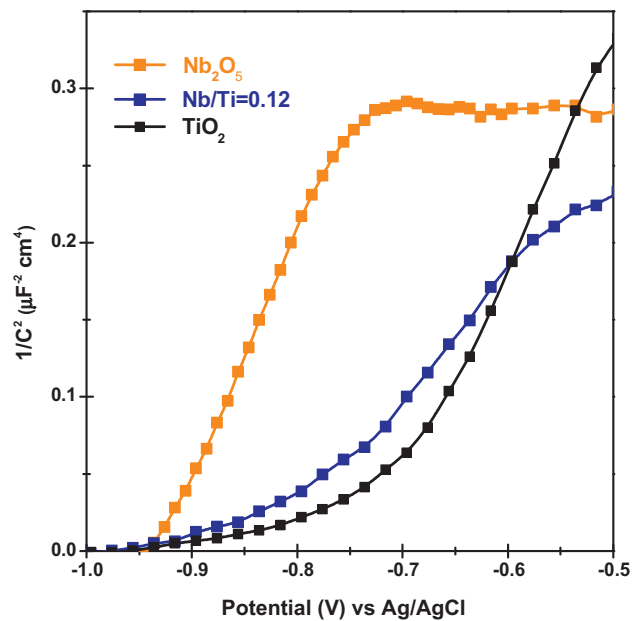


**Fig. 10.** Mott–Schottky plots of  $\text{TiO}_2$ ,  $\text{Nb}_2\text{O}_5$  and  $\text{Nb}_2\text{O}_5/\text{TiO}_2$  heterojunction ( $\text{Nb}/\text{Ti}=0.12$ ) in 0.5 M  $\text{Na}_2\text{SO}_4$ .

(see example of  $\text{Nb}/\text{Ti}=0.12$ ) is smaller than  $\text{TiO}_2$  or  $\text{Nb}_2\text{O}_5$ . According to previous reports [48], the smaller slope suggests a faster charge transfer. That is, the Mott–Schottky plots reveal that the charge transfer ability of  $\text{Nb}_2\text{O}_5/\text{TiO}_2$  hereojunctions is higher than  $\text{TiO}_2$  and  $\text{Nb}_2\text{O}_5$ , which will contribute to the higher photocatalytic activity.

When the heterojunctions are used in photocatalytic reduction reaction, e.g. photo-catalytic methanol reforming (reduction of  $\text{H}^+$  to  $\text{H}_2$ ), the photo-generated electrons will transfer from the conduction band of  $\text{Nb}_2\text{O}_5$  to rutile  $\text{TiO}_2$  and reduce  $\text{PtCl}_6^{2-}$  to Pt sites on the surface of  $\text{TiO}_2$ , which subsequently act as the photocatalytic reduction sites. When the heterojunctions are used in photo-oxidation reaction, e.g. photocatalytic  $\alpha$ -phenylethanol oxidation, the photo-generated holes will transfer from the valence band of  $\text{TiO}_2$  to  $\text{Nb}_2\text{O}_5$  and the small  $\text{Nb}_2\text{O}_5$  nanoparticles will act as the photo-catalytic oxidation sites. Obviously, different sites are involved in the photocatalytic oxidation and reduction reactive reaction.

As a whole, it can be concluded that the as-prepared  $\text{Nb}_2\text{O}_5/\text{TiO}_2$  heterojunctions system is suitable not only for photo-catalytic alcohol oxidation but also for proton reduction owing to the relative position of the conduction and valance band of the two components. While more significant promotion effect can be observed for photocatalytic alcohol oxidation due to the direct involvement of  $\text{Nb}_2\text{O}_5$  nanoparticles in the reaction.

#### 4. Conclusion

Ultra-fine  $\text{Nb}_2\text{O}_5$  nanoparticles are successfully *in situ* loaded on rutile  $\text{TiO}_2$  surface through a simple direct hydrolysis route under strong acidic conditions. Characterization results indicate that electron-rich amorphous niobium oxides of ca. 2 nm are well dispersed on the surface of  $\text{TiO}_2$  and  $\text{Nb}_2\text{O}_5/\text{TiO}_2$  heterojunctions are formed, which can greatly promote the separation efficiency of photo-generated electron–hole pairs under irradiation.

$\text{Nb}_2\text{O}_5/\text{TiO}_2$  heterojunctions exhibit remarkable photocatalytic activity, apparently higher than pure rutile  $\text{TiO}_2$  or  $\text{Nb}_2\text{O}_5$ , in both the selective oxidation of  $\alpha$ -phenylethanol and the hydrogen evolution from methanol reforming. The photocatalytic activity of  $\text{Nb}_2\text{O}_5/\text{TiO}_2$  heterojunctions is dependent on Nb/Ti ratio and

the optimized activity can be obtained at Nb/Ti = 0.12, basically in accordance with the separation efficiency of photo-generated electron-hole pairs. The relative band edge positions between amorphous Nb<sub>2</sub>O<sub>5</sub> and rutile TiO<sub>2</sub> are theoretically predicted and further confirmed by Mott–Schottky plots. According to the results, the photo-generated electrons in the conduction band of Nb<sub>2</sub>O<sub>5</sub> will transfer to rutile TiO<sub>2</sub>, and the photo-generated holes are reversely transferred under the driving force of Fermi energy difference between the two semiconductors. In this context, Nb<sub>2</sub>O<sub>5</sub> nanoparticles in Nb<sub>2</sub>O<sub>5</sub>/TiO<sub>2</sub> heterojunctions act as oxidation sites and uncovered TiO<sub>2</sub> surfaces act as reduction sites in photocatalytic reactions.

## Acknowledgements

We would like to thank Prof. Jinlong Gong at Tianjin University for the help on Mott–Schottky study. This work is supported by the Collaborative Innovation Center of Chemical Science and Engineering (Tianjin). The financial supports from 111 Project (B12015) and the Ministry of Education of China (NCET-11-0251, IRT13022) are also acknowledged.

## Appendix A. Supplementary data

Supplementary material related to this article can be found, in the online version, at <http://dx.doi.org/10.1016/j.apcatb.2014.01.049>.

## References

- [1] A. Fujishima, K. Honda, *Nature* 238 (1972) 37–38.
- [2] X.B. Chen, S.S. Mao, *Chem. Rev.* 107 (2007) 2891–2959.
- [3] L. Thompson, J.T. Yates, *Chem. Rev.* 106 (2006) 4428–4453.
- [4] M. Anpo, M. Takeuchi, *J. Catal.* 216 (2003) 505–516.
- [5] J. Yan, G. Wu, N. Guan, L. Li, Z. Li, X. Cao, *Phys. Chem. Chem. Phys.* 15 (2013) 10978–10988.
- [6] F. Zhang, R. Jin, J. Chen, C. Shao, W. Gao, L. Li, N. Guan, *J. Catal.* 232 (2005) 424–431.
- [7] J. Yang, D. Wang, H. Han, C. Li, *Acc. Chem. Res.* 46 (2013) 1900–1909.
- [8] E.S. Kim, N. Nishimura, G. Magesh, J.Y. Kim, J.W. Jang, H. Jun, J. Kubota, K. Domen, J.S. Lee, *J. Am. Chem. Soc.* 135 (2013) 5375–5383.
- [9] M. Long, W. Cai, J. Cai, B. Zhou, X. Chai, Y. Wu, *J. Phys. Chem. B* 10 (2006) 20211–20216.
- [10] A. Kudo, Y. Miseki, *Chem. Soc. Rev.* 38 (2009) 253–278.
- [11] S.J. Hong, S. Lee, J.S. Jang, J.S. Lee, *Energy Environ. Sci.* 4 (2011) 1781–1787.
- [12] X.F. Gao, W.T. Sun, Z.D. Hu, G. Ai, Y.L. Zhang, S. Feng, F. Li, L.M. Peng, *J. Phys. Chem. C* 113 (2009) 20481–20485.
- [13] C.J. Li, P. Zhang, R. Lv, J.W. Lu, T. Wang, S.P. Wang, F.H. Wang, J.L. Gong, *Small* 9 (2013) 3951–3956.
- [14] J.S. Zhang, M.W. Zhang, R.Q. Sun, X.C. Wang, *Angew. Chem. Int. Ed.* 51 (2012) 10145–10149.
- [15] W.F. Yao, B. Zhang, C.P. Huang, C. Ma, X.L. Son, Q.J. Xu, *J. Mater. Chem.* 22 (2012) 4050–4055.
- [16] L.C. Liu, X.R. Gu, C.Z. Sun, H. Li, Y. Deng, F. Gao, L. Dong, *Nanoscale* 4 (2012) 6351–6359.
- [17] P. Chen, L. Gu, X.B. Cao, *CrystEngComm* 12 (2010) 3950–3958.
- [18] H.L. Lin, H.F. Ye, B.Y. Xu, J. Cao, S.F. Chen, *Catal. Comm.* 37 (2013) 55–59.
- [19] Y. Zhao, C. Eley, J.P. Hu, J.S. Foord, L. Ye, H.Y. He, S.C. Edman Tsang, *Angew. Chem. Int. Ed.* 51 (2012) 3846–3849.
- [20] T. Ohuchi, T. Miyatake, Y. Hitomi, T. Tanaka, *Catal. Today* 120 (2007) 233–239.
- [21] A.G.S. Prado, L.B. Bolzon, C.P. Pedroso, A.O. Moura, L.L. Costa, *Appl. Catal. B* 82 (2008) 219–224.
- [22] H.Y. Lin, H.C. Yang, W.L. Wang, *Catal. Today* 174 (2011) 106–113.
- [23] S.T. Aruna, S. Tirosh, A. Zaban, *J. Mater. Chem.* 10 (2000) 2388–2391.
- [24] H.L. Ma, J.Y. Yang, Y. Dai, Y.B. Zhang, B. Lu, G.H. Ma, *Appl. Surf. Sci.* 253 (2007) 7497–7500.
- [25] C.D. Wagner, W.M. Riggs, L.E. Davis, J.F. Moulder, G.E. Muilenberg, *Handbook of X-ray Photoelectron Spectroscopy: A Reference Book of Standard Data for Use in X-ray Photoelectron Spectroscopy*, Eden-Prairie, Perkin-Elmer MN, 1979.
- [26] V.L.S.T. da Silva, M. Schmal, S.T. Oyama, *J. Solid State Chem.* 123 (1996) 169–182.
- [27] P.V. Kamat, *J. Phys. Chem. Lett.* 3 (2012) 663–672.
- [28] S. Furukawa, T. Shishido, K. Teramura, T. Tanaka, *ACS Catal.* 2 (2012) 175–179.
- [29] F.X. Zhang, N.J. Guan, Y.Z. Li, X. Zhang, J.X. Chen, H.S. Zeng, *Langmuir* 19 (2003) 8230–8234.
- [30] B. Ohtani, Y. Okugawa, S. Nishimoto, T. Kaguya, *J. Phys. Chem.* 91 (1987) 3550–3555.
- [31] A. Suksal, J. Aarik, H. Mandar, I. Sildos, *Thin Solid Films* 336 (1998) 295–298.
- [32] B. Liu, X. Zhao, Q. Zhao, X. He, J. Feng, *J. Electron Spectrosc. Relat. Phenom.* 148 (2005) 158–163.
- [33] R.E. Rex, F.J. Knorr, J.L. McHale, *J. Phys. Chem. C* 117 (2013) 7949–7951.
- [34] W. Feng, G.J. Wu, L.D. Li, N.J. Guan, *Green Chem.* 13 (2011) 3265–3272.
- [35] Y. Shiraiishi, D. Tsukamoto, Y. Sugano, A. Shiro, S. Ichikawa, S. Tanaka, T. Hirai, *ACS Catal.* 2 (2012) 1984–1992.
- [36] J. Yan, G. Wu, N. Guan, L. Li, *Chem. Commun.* 49 (2013) 11767–11769.
- [37] J. Zhang, Q. Xu, Z.C. Feng, M.J. Li, C. Li, *Angew. Chem. Int. Ed.* 47 (2008) 1766–1769.
- [38] K. Sayama, H. Arakawa, K. Domen, *Catal. Today* 28 (1996) 175–182.
- [39] I. Nowak, M. Ziolk, *Chem. Rev.* 99 (1999) 3603–3624.
- [40] D. Robert, *Catal. Today* 122 (2007) 20–26.
- [41] H.L. Luo, W.J. Song, P.G. Hoertz, K. Hanson, R. Ghosh, S. Rangan, M.K. Brenneman, J.J. Concepcion, R.A. Binstead, R. Bartynski, R. Lopez, T.J. Meyer, *Chem. Mater.* 25 (2013) 122–134.
- [42] M.A. Butler, D.S. Ginley, *J. Electrochem. Soc.* 125 (1978) 228–232.
- [43] Y.I. Kim, S.J. Atherton, E.S. Brigham, T.E. Mallouk, *J. Phys. Chem.* 97 (1993) 11802–11810.
- [44] J. Tersoff, *Phys. Rev. B* 30 (1984) 4874–4877.
- [45] H. Huang, D. Li, Q. Lin, Y. Shao, W. Chen, Y. Hu, Y. Chen, X. Fu, *J. Phys. Chem. C* 113 (2009) 14264–14269.
- [46] Y. Jia, S. Shen, D. Wang, X. Wang, J. Shi, F. Zhang, H. Han, C. Li, *J. Mater. Chem. A* 1 (2013) 7905–7912.
- [47] S.R. Morrison, *Electrochemistry at Semiconductor and Oxidized Metal Electrodes*, Plenum Press, New York, 1980 (Chapter 4).
- [48] F. Su, T. Wang, R. Lv, J. Zhang, P. Zhang, J. Lu, J. Gong, *Nanoscale* 5 (2013) 9001–9009.